

F Doped δ -MnO₂ Nanoflowers for High-Performance Aqueous Zinc-Ion Batteries

Zhou Li,^[a] Zhongqiang Ye,^[a] Guangzhan Liu,^[a] Ziyan Jiang,^[a] Wenjia Jiang,^[a] Junwei Luo,^[a] Shaoxiong Liu,^[a] Hai Hu,^[a] Zhifeng Huang,^{*[a]} and Li Liu^{*[a]}

Aqueous zinc-ion batteries (AZIBs) have attracted significant attention from researchers in recent years due to their low cost, high safety and high theoretical capacity. Among them, δ -MnO₂ is considered one of the most promising cathode materials for aqueous zinc ion batteries because of its layered structure, which facilitates the intercalation and deintercalation of zinc ions. However, its narrow layer spacing and poor structural stability limit its future practical applications. To tackle these issues, herein, we report a two-step strategy to introduce anionic fluoride ions into the δ -MnO₂ nanoflowers. The flower-like spherical structure, composed of interspersed nanosheets,

increases the active sites for electrochemical reactions. Fluorine doping can expand the interlayer spacing available for ion insertion/extraction, and the formed fluorine-manganese chemical bonds could stabilize the manganese-oxygen octahedral ($[\text{MnO}_6]$) structure. The F-doped δ -MnO₂ nanoflowers show a reversible capacity of 435.1 mAh g⁻¹ at a current density of 0.1 A g⁻¹, which is obviously higher than that of undoped δ -MnO₂ (212 mAh g⁻¹). These results indicate the potential of anion introduction in enhancing the electrochemical performance of δ -MnO₂ in aqueous zinc-ion batteries.

1. Introduction

In recent years, with the continued depletion of fossil energy reserves, highly efficient energy storage devices have been developed and used to reduce dependence on traditional fossil energy sources.^[1] Lithium-ion batteries (LIBs) currently dominate the energy storage market due to their high energy density and operating voltage. However, the rare and expensive condition of lithium metal resources, the toxic and flammable hazards of organic electrolytes, and the environmental pollution caused by the disposal of lithium batteries make it necessary to find alternative, safe, and reliable energy storage devices.^[2] Therefore, it is urgent to explore other safe, reliable, and economical materials or types of batteries. Among the many candidates,^[3] reversible aqueous zinc-ion batteries (AZIBs) stand out from many alternatives due to their abundant resources, low cost, high safety, high theoretical capacity of Zn (820 mAh g⁻¹), low oxidation-reduction potential (-0.76 V vs. standard hydrogen electrode), and environmental friendliness.^[4]

The cathode material is a crucial component of the battery system and significantly impacts its performance. Among the various cathode materials under investigation for AZIBs,^[5] transition metal oxides, especially manganese dioxide, are widely favored by researchers due to their innate advantages of

diverse crystalline types, ease of preparation and high theoretical capacity (308 mAh g⁻¹).^[6] Birnessite-type MnO₂ (δ -MnO₂) with a layered structure is regarded as one of the most ideal cathode materials for AZIBs due to the large layer spacing between its own structures (~0.7 nm). This kind of spacing is conducive to the rapid detachment and embedding of zinc ions and faster reaction kinetics.^[7] Among the different crystal types of manganese dioxide (α , β , γ , δ , etc.), δ -MnO₂ is the preferred choice.^[8] However, the practical research tests of the material have shown unsatisfactory capacity and cycling stability. This is mainly due to poor intrinsic ionic conductivity, phase transition, and structural collapse during cycling, as well as the active component's dissolution effect in the electrolyte during the charging and discharging phases. To improve the electrochemical properties of materials, various methods are employed, including surface modification, nano-structural design, defect engineering, composite construction, ion doping, and so on. Long et al. doped Cu and Bi cations into δ -MnO₂ through one-step hydrothermal to improve the specific capacity and cycling stability of the material.^[9] Additionally, other metal cations, such as Al³⁺, Na⁺ and so on, were introduced or doped into the MnO₂ ordinary material to expand the lattice spacing and enhance the ion transport rate in the cathode material, thereby improving the electrochemical properties of the material.^[10] The researchers have produced numerous reports on cation doping in the past few years. However, there have been few reports on the introduction of anions into manganese dioxide to investigate whether this process can improve the structure and electrochemical properties of the material.

Herein, F doped δ -MnO₂ nanoflowers are synthesized using a two-step method. The introduced F⁻ can partially replace O²⁻ to increase the material's conductivity and improve its ionic transport ability. Additionally, the fluorine-manganese bond formed between the introduced fluorine and the original

[a] Z. Li, Z. Ye, G. Liu, Z. Jiang, W. Jiang, J. Luo, S. Liu, H. Hu, Z. Huang, L. Liu
Key Laboratory of Environmentally Friendly Chemistry and Applications of Ministry of Education, National Local Joint Engineering Laboratory for Key materials of New Energy Storage Battery, Hunan Province Key Laboratory of Electrochemical Energy Storage and Conversion, School of Chemistry, Xiangtan University, Xiangtan 411105, China
E-mail: liulili1203@126.com
zhifeng_h@126.com

 Supporting information for this article is available on the WWW under <https://doi.org/10.1002/batt.202400660>

manganese can stabilize the manganese-oxygen octahedral structure, effectively reducing the dissolution of manganese during the electrode cycling. When used as cathode for AZIBs, F doped $\delta\text{-MnO}_2$ nanoflowers exhibit excellent multiplicity performance, which can provide an ultra-high capacity of 435.1 mAh g^{-1} at 0.1 A g^{-1} and stable cycle for more than 200 circles at 0.5 A g^{-1} . This kind of simple and effective method of anion doping provides a new idea and strategy for designing advanced energy storage materials and introducing more types of anions.

Experimental

Synthesis of Cathode Materials

The preparation process of FMO is shown in Figure 1. Typically, KMnO_4 and MnSO_4 (molar ratio 6:1) were placed into a PTFE liner containing 50 ml of distilled water and the solution was magnetically stirred for 1 hr. The liner was then placed in a stainless steel reactor and then transferred to an oven to be heated to 160°C for 12 hours. Once the temperature had reached room temperature, the black-brown precipitate in the liner was washed by centrifugation alternately with distilled water and ethanol for 4 times and dried in the oven at 60°C for 12 h to get a powder that is $\delta\text{-MnO}_2$. The obtained $\delta\text{-MnO}_2$ was mixed with an appropriate amount of NH_4F in 100 ml of deionized water, and then dried with stirring at 70°C . Finally, the material was calcined in a muffle furnace at 200°C for 6 h, resulting in the formation of F doped $\delta\text{-MnO}_2$, which is denoted as FMO.

Materials Characterization

The morphology and microstructural properties of the obtained samples were observed by field emission scanning electron microscope FESEM (JEOL, JSM-IT700HR) and field emission transmission electron microscope TEM (FEI, Tecnai G2 F20 S-TWIN). The physical phase analysis and crystal structure of the prepared samples were examined by X-ray diffraction XRD (Rigaku, MiniFlex600). The surface composition and elemental valence of the prepared samples were analyzed by X-ray photoelectron spectroscopy XPS (ULVAC-PHI, PHI VersaProbe 4). The specific surface area, pore structure, and pore size distribution of the prepared materials were evaluated by a fully automated specific surface and porosity analyzer BET (Quantachrome-EVO).

Electrochemical Characterization

The ZIBs were fabricated using a CR2032-type coin cell, and the prepared sample material was used as the cathode of the battery, metal zinc foil (0.01 mm thickness and 15 mm diameter) as the anode of the battery, glass fiber paper as the diaphragm, and the

mixture solution of 2 M zinc sulphate (ZnSO_4) and 0.2 M manganese sulphate (MnSO_4) as the electrolyte. The electrode slurry was prepared by combining each sample materials, conductive carbon black, and polyvinylidene difluoride (PVDF) in the ratio of 7:2:1 in the appropriate amount of N-methyl-2-pyrrolidone (NMP), and then uniformly coated on the stainless steel mesh with a brush. Subsequently, the stainless steel mesh was subjected to vacuum drying at a temperature of 60°C for a period of 12 hours, the active substance loadings of the electrode was fixed about $1.2\text{--}1.5 \text{ mg cm}^{-2}$. The cyclic voltammetry (CV) curves and electrochemical impedance spectra (EIS) were obtained via the electrochemical workstation, where the EIS was obtained at a 5 mv AC signal with a frequency range of 10^{-3} to 10^5 Hz . The specific capacity, rate performance, and cycling stability of the AZIBs were monitored by using a Neware battery tester in the voltage range of 1.0–1.8 V (vs. Zn/Zn^{2+}). The ion diffusion coefficients of the cells were also calculated and evaluated using constant current intermittent titration (GITT).

2. Results and Discussion

In order to investigate the crystal structure of the materials, X-ray diffraction (XRD) measurements were conducted and the results are presented in Figure 2a. The principal diffraction peaks of both $\delta\text{-MnO}_2$ and FMO can be attributed to the standard card of $\delta\text{-MnO}_2$ (JCPDS No. 13-0105), indicating that the doping of F^- does not destroy the crystal structure of the original $\delta\text{-MnO}_2$. It is noteworthy that Figure 2d reveals a slight leftward shift in the position of the (001) peak of FMO with respect to $\delta\text{-MnO}_2$ after the introduction of F^- . This indicates that the layer spacing of the material becomes larger after the doping of F^- . This may be due to the electronegativity of F^- is higher than that of O^{2-} , so appropriate substitution of O^{2-} with F^- can promote a tighter binding between transition metals and oxygen, leading to the increase the interlayer spacing between manganese oxide layers.^[11] The increased layer spacing is important for increasing the Zn^{2+} diffusion kinetics, which is also very important for improving the electrochemical performance of FMO. As can be observed in the scanning electron microscope (SEM) images in Figure 2b-c and e-f, it can be observed that both $\delta\text{-MnO}_2$ and FMO exhibit similar flower-like nanostructures, which are composed by intertwining of two-dimensional nanosheets.

Additionally, by comparing the HRTEM images of $\delta\text{-MnO}_2$ and FMO (Figure 3c and Figure 3f), it can be observed that the lattice spacing of the FMO (001) crystal plane is 0.7 nm, while the $\delta\text{-MnO}_2$ is 0.68 nm, indicating that the introduction of fluorine significantly increases the lattice spacing, providing a

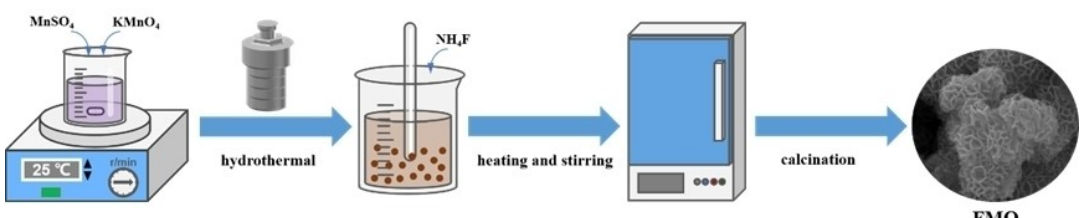


Figure 1. Schematic diagram for the synthesis of FMO.

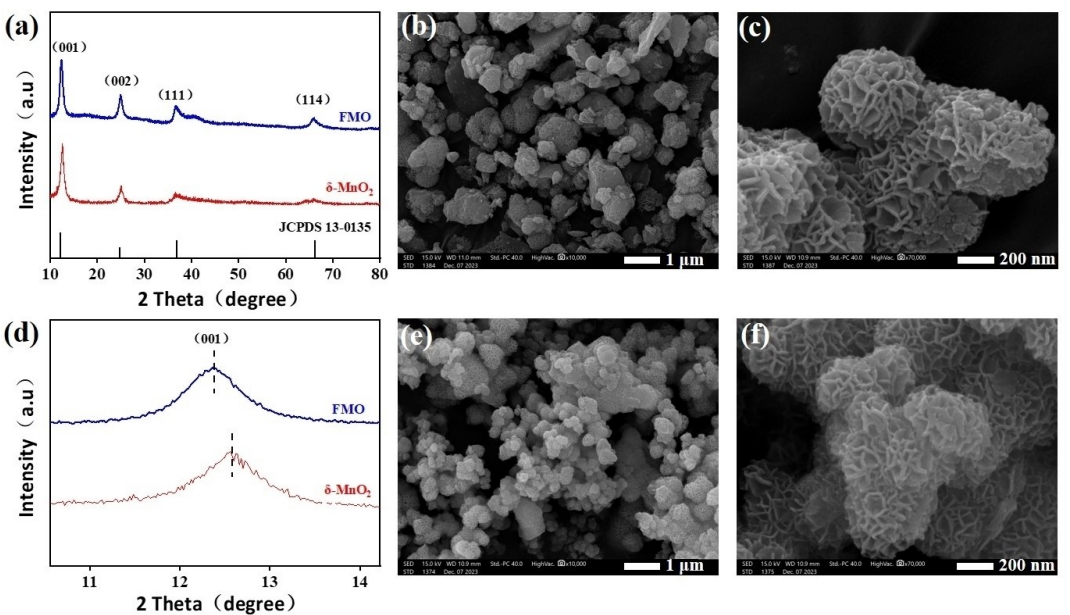


Figure 2. (a) the XRD patterns of FMO and δ -MnO₂; (b–c) the SEM images of δ -MnO₂; (d) the (001) crystal magnification XRD patterns; (e–f) the SEM images of FMO.

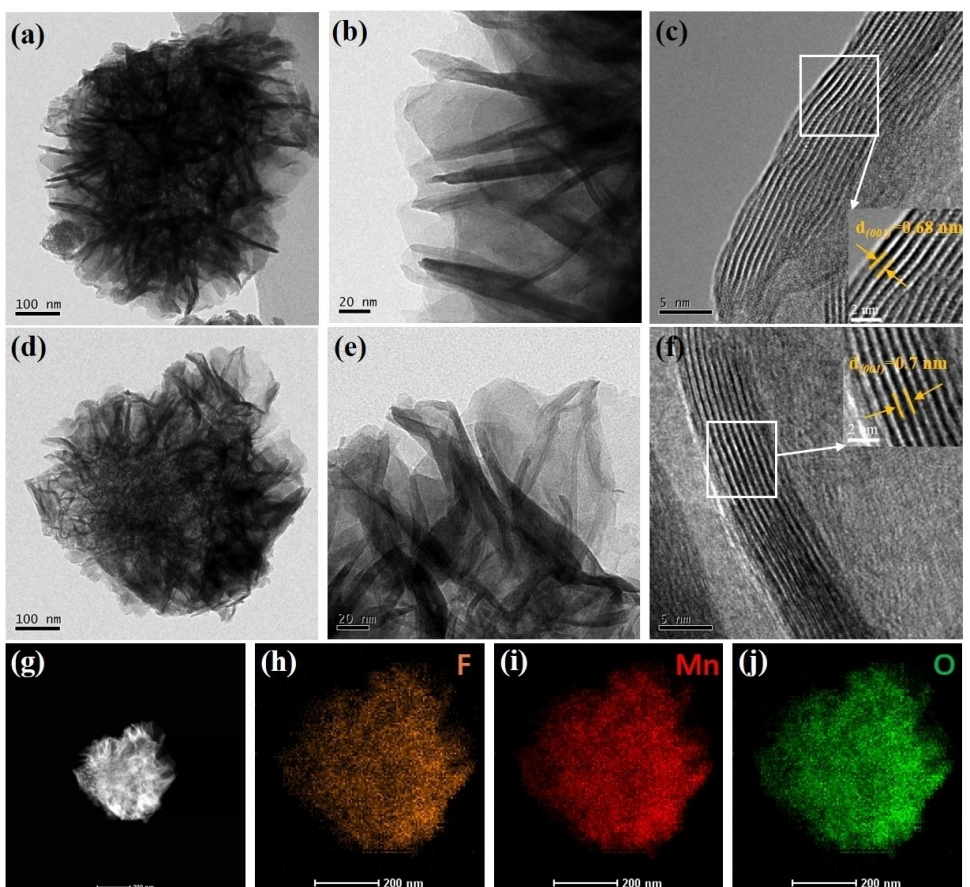


Figure 3. (a–b) the TEM images and (c) the HRTEM images of δ -MnO₂; (d–e) the TEM images and (f) the HRTEM images of FMO; (g–j) the F, Mn, and O elemental mapping images of FMO.

faster channel for the transfer of conductive ions between the electrolyte and the positive electrode. Moreover, Figure 3d–e

further confirm that FMO is composed of numerous interconnected nanosheets forming flower-like spheres, consistent with

the SEM images of FMO. The uniform distribution of the elements Mn, O and F within the FMO is shown by energy dispersive X-ray spectroscopy (EDS) in Figure 3g-j. This observation underscores the successful incorporation of F ions into the FMO. To further understand the elemental valence states and chemical compositions in δ -MnO₂ and FMO, X-ray photoelectron spectroscopy (XPS) analysis was performed. The XPS full spectra of δ -MnO₂ and FMO are shown in Figure 4a. From the overall spectra and the fine spectrum of F 1 s in Figure 4d, it is evident that FMO contains Mn, O, K, and F elements, thus confirming the successful incorporation of F in FMO, whereas the element of F is absent in δ -MnO₂. The Mn 2p XPS spectrum in Figure 4b reveals a pair of peaks at 642.1 eV (Mn 2p_{3/2}) and 653.7 eV (Mn 2p_{1/2}), with a spin energy difference of 11.6 eV, confirming the features of the manganese dioxide phase.^[12] Upon fitting, four fitting peaks related to Mn³⁺ and Mn⁴⁺ are obtained, indicating the coexistence of mixed valence states of Mn in the materials. Furthermore, a comparison of the Mn 2p spectra of FMO and δ -MnO₂ revealed an increase in the integral area ratio of Mn³⁺/Mn⁴⁺ from 0.66 in δ -MnO₂ to 0.85 in FMO. This suggests that with the introduction of F⁻, the element of Mn in FMO exhibits a lower valence state.^[13] It also means that compared to MnO₂, the content of Mn³⁺ in FMO is increased, this may be due to the introduction of fluoride anions causing the conversion of Mn⁴⁺ to Mn³⁺ to ensure the electronic balance inside the material. Additionally, in the O1s fine spectrum (Figure 4c), FMO can be fitted into three characteristic peaks located at 529.6, 531.3, and 533.1 eV, respectively. Similar peaks are also observed in δ -MnO₂, corresponding to Mn-O-Mn, Mn-OH, and H-O-H bonds, respectively.^[14] The existence of H-O-H and Mn-OH bonds is due to the preparation environment of the material being in aqueous solution, so water molecules will adsorb on the surface of the material and the interlayer between manganese oxide layers.

The Brunauer-Emmett-Teller (BET) specific surface area and pore size distribution of FMO and δ -MnO₂ are depicted in Figure 4e-f. The N₂ adsorption-desorption isotherms indicate that both samples possess IV type mesoporous structures. The pore size distribution chart in Figure 4f illustrates that the pore sizes of both materials are mainly distributed between 2–5 nm. The specific surface areas and total pore volumes of δ -MnO₂ and FMO are listed in Table S1. The surface area of FMO is 28.139 m² g⁻¹, which is significantly higher than that of δ -MnO₂ (19.511 m² g⁻¹). The total pore volume of FMO is also larger than that of δ -MnO₂. The larger surface area of FMO will provide abundant active sites for electrochemical reactions, increasing the contact area between the material and the electrolyte.^[15] This enhances reaction kinetics, thereby improving the electrochemical performance of the FMO.

Figure 5a illustrates the CV curve of FMO and δ -MnO₂ at a scan rate of 0.2 mVs⁻¹ within a voltage window of 1.0–1.8 V. It is evident that FMO exhibits two pairs of distinct oxidation-reduction peaks at high and low potentials, indicating the extraction/insertion of Zn²⁺ and H⁺. The reduction peaks around 1.36 V and 1.24 V can be attributed to the insertion of H⁺ and Zn²⁺, while the oxidation peaks around 1.56 V and 1.61 V result from the extraction of Zn²⁺ and H⁺.^[16] In addition, the peak current and curve area of FMO is significantly larger than those of δ -MnO₂, indicating that the FMO electrode has a higher specific capacity than δ -MnO₂. Figure 5b compares the galvanostatic charge-discharge curves (GCD) of FMO and δ -MnO₂ at a current density of 0.5 Ag⁻¹. As indicated that both samples have two distinct discharge plateaus around 1.4 V and 1.2 V. According to previously reported literature,^[17] the first plateau is attributed to the insertion of H⁺, while the second plateau corresponds to the insertion of Zn²⁺, which is in good agreement with the above CV curves. Furthermore, it can be shown that the specific capacity of FMO (320.7 mAhg⁻¹) is

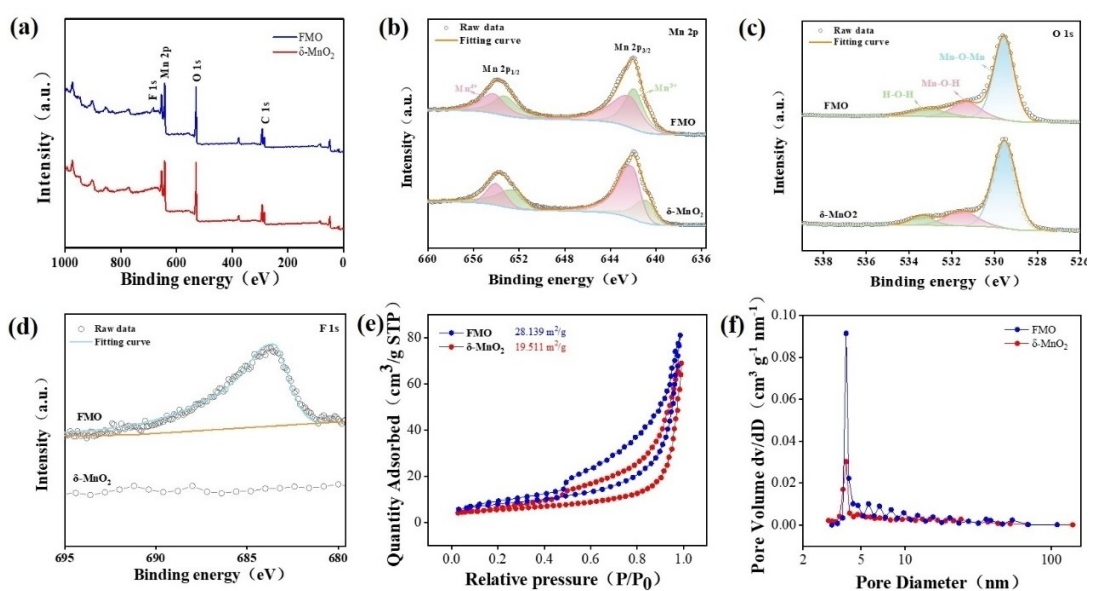


Figure 4. (a) The XPS full spectra of δ -MnO₂ and FMO; (b) the Mn 2p XPS survey spectra; (c) the O 1s XPS survey spectra; (d) the High-resolution F 1s XPS spectra of FMO and δ -MnO₂; (e-f) BET specific surface area and pore size distribution of FMO and δ -MnO₂.

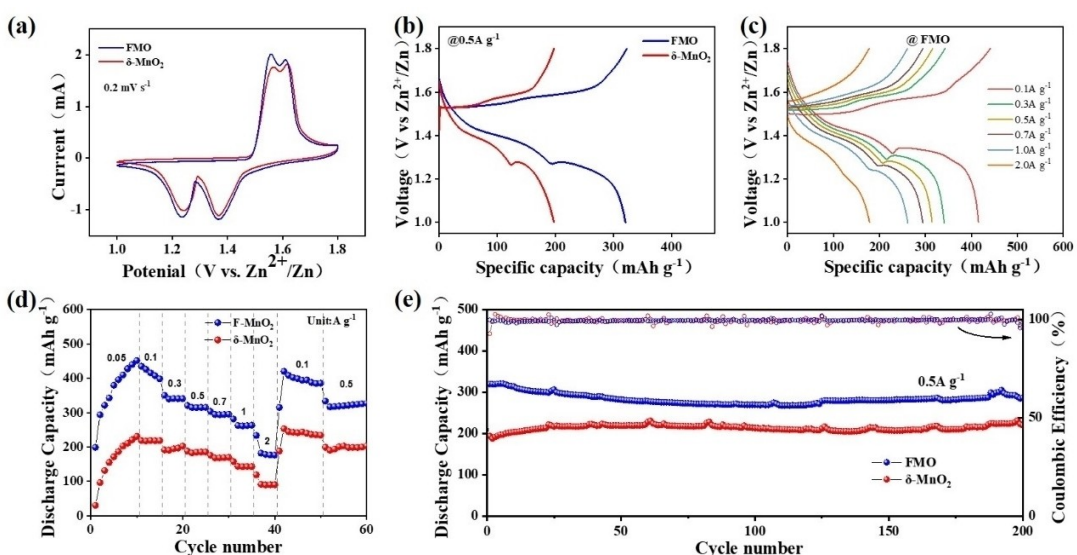


Figure 5. (a) the CV curves of FMO and δ -MnO₂ at 0.2 mV s⁻¹; (b) the GCD curves of FMO vs. δ -MnO₂ at 0.5 A g⁻¹; (c) the GCD curves of FMO at diverse current densities; (d-e) the comparison of rate performance and cycling performance of FMO vs. δ -MnO₂ at 0.5 A g⁻¹.

significantly higher than that of MnO₂ (190.6 mAh g⁻¹) at a current density of 0.5 A g⁻¹, and the voltage difference between the charge and discharge platforms of FMO is significantly smaller than that of MnO₂, indicating that the FMO electrode has a smaller degree of polarization. Figure 5c is the GCD curves of FMO at diverse current densities, which shows that as the current density increases, the charging and discharging platform of FMO still significantly exists. Figure 5d demonstrates the rate capability of FMO and δ -MnO₂ in the current density range of 0.1–2 A g⁻¹, the first 10 cycles are an activation process for electrode materials with a current density of 0.05 A g⁻¹. FMO exhibits outstanding rate capability compared to δ -MnO₂. It delivers high capacities of 435.1, 340.3, 320.7, 290.4, 260.8, and 175.1 mAh g⁻¹ at current densities of 0.1, 0.3, 0.5, 0.7, 1.0, and 2.0 A g⁻¹, respectively. These results are markedly higher than those observed for δ -MnO₂ at the corresponding current densities. In addition, even when the current density returns to 0.1 A g⁻¹ and 0.5 A g⁻¹, the discharge capacity of the FMO cathode electrode can still maintain at 425.6 and 316.6 mAh g⁻¹, respectively. This further demonstrates its preeminent cycling performance and high reversibility. The outstanding rate performance of the FMO electrode may be attributed to its well-defined flower-like morphology formed by interlocked nanosheets and the stabilization of manganese oxide octahedral structure by the introduction of F⁻. Next, the cycling performance of the FMO and δ -MnO₂ cathode electrodes at 0.5 A g⁻¹ is shown in Figure 5e. It can be seen that after 200 cycles, FMO still retains 90% of its original capacity. Moreover, the capacity of FMO is significantly exceed that of δ -MnO₂. This demonstrates that the introduction of F⁻ not only greatly improves the specific capacity but also ensures the cycling stability.

To further investigate the electrochemical kinetics and related mechanisms of the cathode, we conducted CV tests on the FMO electrode at different scan rates (0.2–1.0 mV s⁻¹). As

shown in Figure 6a, with the scan rate increases, the CV curves of FMO maintain the shape and the presence of two pairs of oxidation-reduction peaks (labeled as Peak 1, Peak 2, Peak 3, and Peak 4 in Figure 6a) reasonably well. Some slight peak shifts observed can be attributed to polarization phenomena during ion extraction/insertion processes. In order to better quantify the contributions of diffusion and capacitance control to the capacity of material, we employed the following equations:^[18]

$$i = av^b \# \quad (1)$$

then it can be transformed into:

$$\ln(i) = b\ln(v) + \ln(a) \quad (2)$$

in which i (A) represents the peak current, 'v' denotes the scan rate, and 'a' and 'b' are constants. The constant b is utilized to describe the kinetic information during the electrochemical process, typically ranging from 0.5 to 1. When b equals 0.5, it presents that the process is diffusion-controlled; when b equals 1.0, it presents pseudocapacitive-controlled electrochemical processes^[19]. From Figure 6b, it can be observed that the b values obtained from linear fitting of Peak 1, Peak 2, Peak 3, and Peak 4 are 0.57, 0.78, 0.44, and 0.78, respectively. This indicates that both diffusion control and pseudocapacitive control exist in the FMO electrode, demonstrating a synergistic charge storage behavior. Furthermore, a variation of Equation (1) can further quantify the contribution ratio of pseudocapacitive in the electrochemical process^[20]:

$$i = k_1 v + k_2 v^{\frac{1}{2}} \# \quad (3)$$

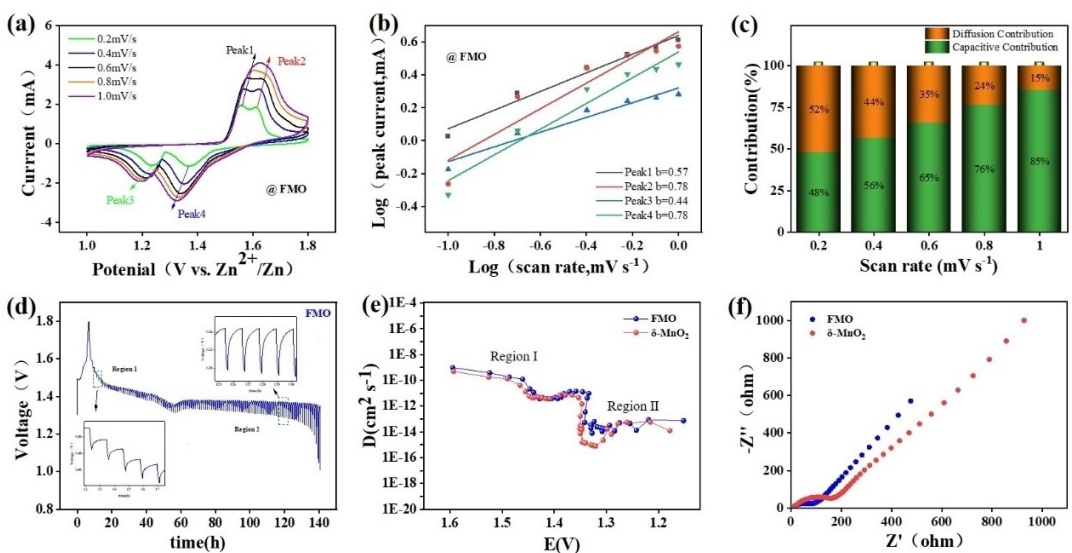


Figure 6. (a) the CV curves of FMO electrode at different scan rates; (b) the plots of $\log(i)$ versus $\log(v)$ at four peaks of FMO electrode; (c) the plots of the ratio of diffusion contribution to pseudocapacitive contribution of the FMO electrode; (d) the GITT curves of the discharge of the FMO electrodes with partial enlarged image; (e) H^+ and Zn^{2+} diffusion coefficients during the discharge of the FMO and $\delta\text{-MnO}_2$ electrode (f) the EIS curves comparison plot of the FMO and $\delta\text{-MnO}_2$.

where $k_1 v$ is the contribution rate of pseudocapacitive behavior, $k_2 v^2$ is the contribution rate of diffusion control behavior^[21]. The calculation results are shown in Figure 6c, indicate that the pseudocapacitive contribution rate of the FMO electrode gradually increases with the increasing scan rate, rising from 48% at 0.2 mV s^{-1} to 85% at 1.0 mV s^{-1} . There is a strong positive correlation between the scan rate and the pseudocapacitive contribution rate. Therefore, the excellent capacitive behavior of the FMO electrode leads to faster ion diffusion, resulting in its outstanding electrochemical performance.

To further elucidate and explore the electrode kinetics and related ion diffusion coefficients of the material, galvanostatic intermittent titration technique (GITT) was employed for quantitative measurement of ion diffusion coefficients. The calculation method is as follows^[22]:

$$D^{GITT} = \frac{4}{\pi \tau} \left(\frac{m_B V_M}{M_B S} \right)^2 \left(\frac{\Delta E_s}{\Delta E_t} \right)^2 \# \quad (4)$$

where τ is the relaxation time (s), m_B is the mass of active material (g), V_M is the molar volume of the electrode material ($\text{cm}^3 \text{ mol}^{-1}$), M_B is the molar mass of the material (g mol^{-1}), the surface area of the electrode in contact with the electrolyte is designated as S (cm^2), ΔE_s is the voltage change between the initial voltage and the final steady-state voltage, and ΔE_t is the voltage change during the charge/discharge process. The battery was discharged or charged at a current density of 0.03 A g^{-1} for 10 minutes and then allowed to rest for 30 minutes to allow the voltage to relax back to a stable state. This process was repeated until the voltage reached 1.0 V or 1.8 V. As a result, the GITT curves of different reaction stages for FMO electrodes, as well as the partial magnifications, are shown

in Figure 6d (the GITT image information about $\delta\text{-MnO}_2$ is depicted in Figure S4 of the supporting information). Figure 6e shows the comparison of ion diffusion coefficients between FMO and $\delta\text{-MnO}_2$ during the discharge process. It can be seen that the introduction of fluoride ions effectively improves the ion diffusion coefficient of FMO, especially in region II, which is extremely obvious, resulting in better electrochemical performance of the FMO electrode compared to the $\delta\text{-MnO}_2$ electrode. Furthermore, it can be observed from Figure 6d that the total overvoltage of the FMO electrode in region II (97.2 mV) is approximately 3.9 times that of region I (24.8 mV), due to the slow ion diffusion in region II caused by the large voltage transition.^[13,23] According to previous reports, the first discharge plateau is attributed to the insertion of H^+ , while the subsequent discharge plateau is attributed to the insertion of Zn^{2+} . Moreover, Figure 6e illustrates that the ion diffusion coefficient of FMO in the first discharge plateau (10^{-11} – $10^{-9} \text{ cm}^2 \text{ s}^{-1}$) is much higher than that in the second discharge plateau (10^{-14} – $10^{-13} \text{ cm}^2 \text{ s}^{-1}$). This further confirms that the energy storage mechanism of the FMO electrode involves multi-step intercalation reactions of the first H^+ insertion and the second Zn^{2+} insertion.

Furthermore, electrochemical impedance spectroscopy (EIS) tests on FMO and $\delta\text{-MnO}_2$ were carried out to further evaluate their ion diffusion ability and charge transfer resistance. The EIS data and corresponding Nyquist plots are presented in Figure 6f, where both curves exhibit similar shapes, presenting a semicircle in the high-frequency region and a straight line in the low-frequency region. The semicircle shape observed in the high-frequency region is indicative of the charge transfer resistance (R_{ct}), while the linear trend in the low-frequency region is attributed to the Warburg impedance (Z_w), representing the diffusion limitation process. This plot aligns well with

the corresponding equivalent circuit diagram (Figure S3). The corresponding fitting data are listed in Table S2, it can be noticed that the charge transfer impedance of the FMO electrode is significantly lower than that of $\delta\text{-MnO}_2$, indicating that the introduction of F^- accelerates the reaction kinetics of the electrode.

3. Conclusions

In summary, F-doped $\delta\text{-MnO}_2$ nanoflowers have been synthesized via a two-step strategy and utilized as a high-performance electrode material for AZIBs. The introduction of fluorine replacing some of the O^{2-} in the material, enlarging the interlayer spacing available for ion insertion/extraction between manganese oxide layers; it also increases the specific surface area of the material, allowing the material to provide more active sites for the redox reactions occurring on the surface. Therefore, F-doped $\delta\text{-MnO}_2$ nanoflowers show better electrochemical activity and faster electrochemical kinetics. The synthesized F-doped $\delta\text{-MnO}_2$ exhibits much better electrochemical properties than the undoped $\delta\text{-MnO}_2$. F-doped $\delta\text{-MnO}_2$ delivers a high capacity of 435.1 mAh g^{-1} at 0.1 A g^{-1} and demonstrates stable rate performance over 200 cycles at 0.5 A g^{-1} . These results provide an effective and reliable strategy for anion doping in manganese dioxide and can serve as a reference for the development of other efficient and high-performance battery materials by introducing anions into other transition metal oxides.

Acknowledgements

This work was supported financially by the National Natural Science Foundation of China (Grant No. 52072325).

Conflict of Interests

The authors declare no conflict of interest.

Data Availability Statement

The data that support the findings of this study are available from the corresponding author upon reasonable request.

Keywords: Fluorine ion doped • Hydrothermal • Nanoflower structure • Aqueous zinc-ion batteries

- [1] a) Y. Liang, H. Dong, D. Aurbach, Y. Yao, *Nat. Energy.* **2020**, *5*, 646–656;
b) G. Fang, J. Zhou, A. Pan, S. Liang, *ACS Energy Letters.* **2018**, *3*, 2480–2501.
- [2] a) C. Meng, S. Knežević, F. Du, Y. Guan, F. Kanoufi, N. Sojic, G. Xu, *eScience.* **2022**, *2*, 591–605; b) Z. P. Cano, D. Banham, S. Ye, A. Hintennach, J. Lu, M. Fowler, Z. Chen, *Nat. Energy.* **2018**, *3*, 279–289;

- c) C. Xu, Y. Chen, S. Shi, J. Li, F. Kang, D. Su, *Sci. Rep.* **2015**, *5*; d) Y. Xu, G. Zhang, J. Liu, J. Zhang, X. Wang, X. Pu, J. Wang, C. Yan, Y. Cao, H. Yang, W. Li, X. Li, *Energy Environ Mater.* **2023**, *6*; e) B. Huang, Z. Sun, G. Sun, *eScience.* **2022**, *2*, 243–277.
- [3] a) Z. Ju, Q. Zhao, D. Chao, Y. Hou, H. Pan, W. Sun, Z. Yuan, H. Li, T. Ma, D. Su, B. Jia, *Adv. Energy Mater.* **2022**, *12*; b) C. Deng, Y. Li, J. Huang, *Small Methods.* **2024**, *8*, e2300832.
- [4] a) W. Yang, W. Yang, Y. Huang, C. Xu, L. Dong, X. Peng, *Chinese Chem. Lett.* **2022**, *33*, 4628–4634; b) Y. Ren, H. Li, Y. Rao, H. Zhou, S. Guo, *Adv. Energy Mater.* **2024**, *17*, 425–441; c) Y. Shang, D. Kundu, J. **2023**, *7*, 244–250; d) N. Naresh, S. Eom, S. J. Lee, S. H. Jeong, J. W. Jung, Y. H. Jung, J. H. Kim, *Adv. Energy Mater.* **2023**; e) B. He, J. Huang, P. Ji, T. K. A. Hoang, M. Han, L. Li, L. Zhang, Z. Gao, J. Ma, J. Zhi, P. Chen, *J. Power Sources.* **2023**, *554*; f) T. Wang, C. Li, X. Xie, B. Lu, Z. He, S. Liang, J. Zhou, *ACS Nano.* **2020**, *14*, 16321–16347; g) C. Liu, X. Xie, B. Lu, J. Zhou, S. Liang, *ACS Energy Letters.* **2021**, *6*, 1015–1033; h) S. Kim, G. Hee Ryu, G. H. An, *Appl Surf Sci.* **2023**, 635.
- [5] a) Y. Li, Z. Wang, Y. Cai, M. E. Pam, Y. Yang, D. Zhang, Y. Wang, S. Huang, *Adv. Energy Mater.* **2022**, *5*, 823–851; b) X. Jia, C. Liu, Z. G. Neale, J. Yang, G. Cao, *Chem. Rev.* **2020**, *120*, 7795–7866.
- [6] a) H. Yao, H. Yu, Y. Zheng, N. W. Li, S. Li, D. Luan, X. W. Lou, L. Yu, *Angew. Chem. Int. Ed.* **2023**, *62*; b) Y. Ma, M. Xu, R. Liu, H. Xiao, Y. Liu, X. Wang, Y. Huang, G. Yuan, *Energy Storage Mater.* **2022**, *48*, 212–222; c) H. Chen, J. Guo, S. Tan, X. Zhang, Z. Sang, D. A. Yang, *Appl Surf Sci.* **2023**, 638.
- [7] Y. Liao, H.-C. Chen, C. Yang, R. Liu, Z. Peng, H. Cao, K. Wang, *Energy Storage Mater.* **2022**, *44*, 508–516.
- [8] a) D. Du, C. Huang, J. Liu, X. Chen, G. Chang, Q. Tang, A. Hu, *Electrochim Acta.* **2023**, *456*; b) R. Han, Y. Pan, C. Du, Y. Xiang, Y. Wang, H. Zhu, C. Yin, *J. Energy Storage.* **2024**, *80*; c) D. Wang, L. Wang, G. Liang, H. Li, Z. Liu, Z. Tang, J. Liang, C. Zhi, *ACS Nano.* **2019**, *13*, 10643–10652; d) X. Gao, H. Wu, W. Li, Y. Tian, Y. Zhang, H. Wu, L. Yang, G. Zou, H. Hou, X. Ji, *Small.* **2020**, *16*.
- [9] F. Long, Y. Xiang, S. Yang, Y. Li, H. Du, Y. Liu, X. Wu, X. Wu, *J. Colloid Interface Sci.* **2022**, *616*, 101–109.
- [10] a) Y. Ding, W. Xue, K. Chen, C. Yang, Q. Feng, D. Zheng, W. Xu, F. Wang, X. Lu, *Nanomaterials (Basel)* **2023**, *13*; b) Z. Wang, K. Han, Q. Wan, Y. Fang, X. Qu, P. Li, *ACS Appl. Mater. Interfaces.* **2023**, *15*, 859–869; c) X. Ding, Y. Wen, C. Qing, Y. Wei, P. Wang, J. Liu, Z. Peng, Y. Song, H. Chen, Q. Rong, *J. Alloy Compd.* **2024**, 986; d) Y. Zhao, S. Zhang, Y. Zhang, J. Liang, L. Ren, H. J. Fan, W. Liu, X. Sun, *Energy Environ. Sci.* **2024**, *17*, 1279–1290.
- [11] S. Kim, B.-R. Koo, Y.-R. Jo, H.-R. An, Y.-G. Lee, C. Huang, G.-H. An, *J. Mater. Chem. A.* **2021**, *9*, 17211–17222.
- [12] W. Sun, F. Wang, S. Hou, C. Yang, X. Fan, Z. Ma, T. Gao, F. Han, R. Hu, M. Zhu, C. Wang, *J. Am. Chem. Soc.* **2017**, *139*, 9775–9778.
- [13] Y. Wang, Y. Zhang, G. Gao, Y. Fan, R. Wang, J. Feng, L. Yang, A. Meng, J. Zhao, Z. Li, *Nano-Micro Letters.* **2023**, *15*.
- [14] D. Wang, Z. Liu, X.-W. Gao, Q. Gu, L. Zhao, W.-B. Luo, *J. Energy Storage.* **2023**, *72*.
- [15] Y. Liu, X. Wu, *Chinese Chem. Lett.* **2022**, *33*, 1236–1244.
- [16] S. Xie, X. Li, Y. Li, Q. Liang, L. Dong, *Chem. Rec.* **2022**, *22*, e202200201.
- [17] a) J. Yang, G. Yao, Z. Li, Y. Zhang, L. Wei, H. Niu, Q. Chen, F. Zheng, *Small.* **2023**, *19*, e2205544; b) K. Sun, J. Pang, Y. Zheng, F. Xing, R. Jiang, J. Min, J. Ye, L. Wang, Y. Luo, T. Gu, L. Chen, *J. Alloy. Compd.* **2022**, 923.
- [18] G. Fang, Z. Wu, J. Zhou, C. Zhu, X. Cao, T. Lin, Y. Chen, C. Wang, A. Pan, S. Liang, *Adv. Energy Mater.* **2018**, *8*, 19.
- [19] S. Liu, H. Zhu, B. Zhang, G. Li, H. Zhu, Y. Ren, H. Geng, Y. Yang, Q. Liu, C. C. Li, *Adv. Mater.* **2020**, *32*, e2001113.
- [20] X. Yang, W. Deng, M. Chen, Y. Wang, C. F. Sun, *Adv. Mater.* **2020**, *32*, e2003592.
- [21] C. Liu, Z. Neale, J. Zheng, X. Jia, J. Huang, M. Yan, M. Tian, M. Wang, J. Yang, G. Cao, *Energy Environ. Sci.* **2019**, *12*, 2273–2285.
- [22] L. Liu, M. Zhou, L. Yi, H. Guo, J. Tan, H. Shu, X. Yang, Z. Yang, X. Wang, *J. Mater. Chem. A* **2012**, *22*, 17539–17550.
- [23] L. Ren, G. Yu, H. Xu, W. Wang, Y. Jiang, M. Ji, S. Li, *ACS Sustain. Chem. Eng.* **2021**, *9*, 12223–12232.

Manuscript received: October 10, 2024

Revised manuscript received: December 4, 2024

Accepted manuscript online: December 8, 2024

Version of record online: December 17, 2024